Size-Controlled Anatase Titania Single Crystals with Octahedron-like Morphology for Dye-Sensitized Solar Cells

Jia-Wei Shiu, Chi-Ming Lan, Yu-Cheng Chang, Hui-Ping Wu, Wei-Kai Huang, and Eric Wei-Guang Diau*

Department of Applied Chemistry and Institute of Molecular Science, National Chiao Tung University, Hsinchu 30010, Taiwan

ABSTRACT A simple hydrothermal method with titanium tetraisopropoxide (TTIP) as a precursor and triethanolamine (TEOA) as a chelating agent enabled growth in the presence of a base (diethylamine, DEA) of anatase titania nanocrystals (HD1−HD5) of controlled size. DEA played a key role to expedite this growth, for which a biphasic crystal growth mechanism is proposed. The produced single crystals of titania show octahedron-like morphology with sizes in a broad range of 30−400 nm; a typical, extra large, octahedral single crystal (HD5) of length 410 nm and width 260 nm was obtained after repeating a sequential hydrothermal treatment using HD3 and then HD4 as a seed crystal. The nanocrystals of size ∼30 nm (HD1) and ∼300 nm (HD5) served as active layer and scattering layer, respectively, to fabricate N719-sensitized solar cells. These HD devices showed greater V_{OC} than devices of conventional nanoparticle (NP) type; the overall device performance of HD attained an efficiency of 10.2% power conversion at a total film thickness of 28 μm, which is superior to that of a NP-based reference device (η = 9.6%) optimized at a total film thickness of 18−20 μm. According to results obtained from transient photoelectric and charge extraction measurements, this superior performance of HD devices relative to their NP counterparts is due to the more rapid electron transport and greater TiO_2 potential.

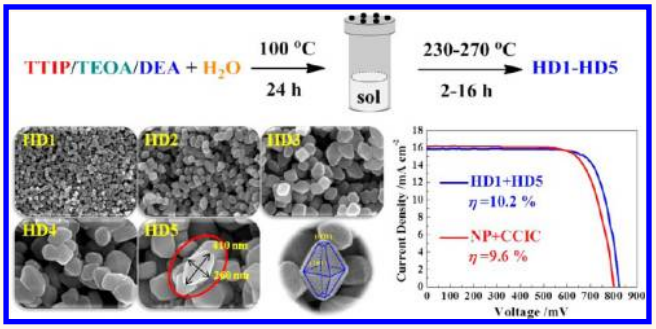

KEYWORDS: anatase · crystal growth · dye-sensitized solar cells · hydrothermal · titania

Nanostructured TiO_2 is of great interest to researchers because the related materials have been utilized in many applications such as photocatalysis, sensors, batteries, photovoltaics, water splitting, and so forth.[1,2] In particular, TiO_2 plays a key role as a mediator of electron transport in working electrodes for dye-sensitized solar cells (DSSCs);[3−6] in such cells, dye molecules are sensitized on the surface of TiO_2 films. Photoexcitation of the dye produces an effective charge separation through rapid injection of electrons from the excited state of the dye into the conduction band of TiO_2; these injected electrons in TiO_2 subsequently migrate toward the electrode, with minimal loss through charge recombination, to generate sufficient photocurrents for the device. An ideal TiO_2 film should thus have adequate porosity and a large specific surface area to attain dye loading (DL) to a sufficient extent and for feasible transport of the redox couple of the electrolyte across the network of mesoporous particles.[4,5] To fulfill the functionality of such TiO_2, the effects of particle size,[7−11] particle shape,[12−18] film composition,[19−23] morphology,[24−32] crystalline phase,[33−35] and peptization condition[36] on photovoltaic performance of the device have been investigated.

For typical highly efficient DSSCs, the TiO_2 films feature a double-layer structure: a scattering layer (SL) with a thickness of 2−5 μm on top of a transparent TiO_2 active layer (AL) with a thickness of 12−14 μm.[5−9,37−40] For an AL, anatase TiO_2 nanoparticles of size ∼20 nm exhibit optimal dye adsorption and light harvesting in the visible spectral region; for SL, the size of particles was increased to 200−400 nm to enhance the light harvesting in the wavelength region of 600−800 nm. Although a TiO_2 SL advantageously

* Address correspondence to diau@mail.nctu.edu.tw.

Received for review September 14, 2012 and accepted November 1, 2012.

Published online November 01, 2012
10.1021/nn3042418

improves the light-harvesting ability of the dye, particles of large size and small surface area would decrease the DL on TiO_2 films. To combine both a dye-loading ability and the light-scattering effect in one TiO_2 layer, various hierarchical pore structures were developed. For instance, Caruso and Cheng[25−27] reported mesoporous spherical TiO_2 beads of size 830 nm, Lee and Park[22] reported mesoporous TiO_2 hollow spheres with a spherical size of 1−3 μm and a wall thickness of ∼250 nm, and Hore *et al.*[21] and Han *et al.*[23] reported interstitial voids in nanocrystalline films. These hierarchical TiO_2 beads and spheres are composed of nanoparticles in the anatase phase of size ∼20 nm so that they exhibited an excellent bifunctional character (AL + SL) for use as photoanodes to promote the overall performance of the DSSCs. Hierarchical anatase TiO_2 mesospheres consisting of various nanostructures, such as nanorods,[24] nanocubes,[16] and nanosheets,[17] were also reported for DSSC applications.

Various methods exist for synthesis of TiO_2 nanostructures of controlled shape and tunable size.[1,2] As a SL for DSSCs, for instance, monodisperse mesoporous TiO_2 spheres were produced in a two-step synthesis comprising a controlled sol−gel process and a hydrothermal or solvothermal treatment with titania precursor at a varied molar ratio in water under basic conditions.[8,9] In a typical hydrothermal approach, various experimental conditions such as titanium precursor, concentration, peptizer, catalyst, surfactant or additive, pH, autoclaving temperature, and duration must be considered to synthesize appropriate anatase TiO_2 nanoparticles as AL for DSSCs. Grätzel and co-workers reported that the size and morphology of the TiO_2 nanoparticles differ when an autoclave was used with varied pH;[3,41] not only were the nanoparticles larger under basic condition than under acidic conditions, but also rod-like[3,41] and octahedral[3,15] nanostructures were observed in the former case. The formation of octahedral or truncated octahedral nanocrystals was observed also under acidic hydrothermal conditions[18,42−44] or non-aqueous solvothermal treatments in the presence of capping surfactants.[45−47] The morphology of a truncated octahedral single crystal is controllable on varying the concentration of the hydrofluoric acid solution to adjust the fraction of reactive {001} facets with respect to the eight thermodynamically stable {101} facets;[18,48,49] the best performance of a device correlated directly with the greatest portion of exposed (001) facets.[16−18]

Even though hydrofluoric acid played a key role as a surface-capping agent in the hydrothermal treatment to control the crystallography and morphology of TiO_2,[18,48,49] using concentrated HF raises serious concerns about hazard to the environment and health due to its toxic and corrosive nature. Hore and Durrant[36] found that devices with TiO_2 films prepared under basic conditions exhibited smaller dark currents and greater open-circuit voltage (V_{OC}) than those prepared under acidic conditions. Accordingly, we developed a simple two-step sol/hydrothermal approach using titanium tetraisopropoxide (TTIP) as a precursor and triethanolamine (TEOA) as a chelating agent to retard the hydrolysis.[50,51] We thus grew anatase titania nanocrystals of controlled size in the presence of a base, diethylamine (DEA), that played a key role expediting the nanocrystal growth in the hydrothermal treatment; the produced titania single crystals show octahedron-like morphology and size of 30−400 nm. The significance of the present work is emphasized on the shape control of the titania nanocrystals using the selective crystal face etching method under a basic condition. The ∼30 nm nanocrystals (denoted HD1) and ∼300 nm nanocrystals (HD5) were fabricated into N719-based DSSCs as AL and SL, respectively. These HD devices showed significantly greater V_{OC} than those of the reference devices (denoted NP) for which the TiO_2 films were fabricated according to a conventional acid-peptized hydrothermal procedure.[40] The performance of the HD devices improved on increasing the thickness of AL, attaining an efficiency η = 10.2% of power conversion optimized at total film thickness 28 μm (SL ∼ 5 μm); this performance is superior to that of the NP device, for which η = 9.6%, optimized at total film thickness of 18−20 μm. To understand the electron transport and charge recombination properties of the system, we undertook transient photoelectric measurements of three relevant devices.

RESULTS AND DISCUSSION

Morphology and Crystallinity. Figure 1 shows SEM images of the morphologies of titania nanocrystals generated from the two-step sol/hydrothermal procedures with varied autoclaving temperature and duration. When we examined the effect of autoclaving period at the fixed temperature of 230 °C, we found that the average particle size increased from ∼30 nm at 2 h (HD1, Figure 1a) to 50−70 nm at 8 h (Figure 1b). The average size did not change further at 16 h (Figure 1c), but some large crystals were observed at extended durations. Concerning the effect of autoclave temperature at fixed duration of 12 h, for temperature increase from 230 °C (Figure 1d) to 250 °C (HD2, Figure 1e) to 270 °C (Figure 1f), the average particle size increased significantly from ∼50 nm to over 100 nm. Moreover, the geometry of the titania nanocrystals varied from a cuboid-like shape at 230 °C to the octahedron-like shape at 270 °C. As shown in Figure 1g for crystals grown at 270 °C for 16 h, larger octahedral or truncated octahedral nanocrystals (HD3) were unambiguously observed. With HD3 as a seed crystal to repeat the same sol/hydrothermal experiment as for HD3, much larger titania single crystals (HD4, Figure 1h) were obtained. Repeating again the experiment with HD4 as a seed crystal, even larger truncated octahedral

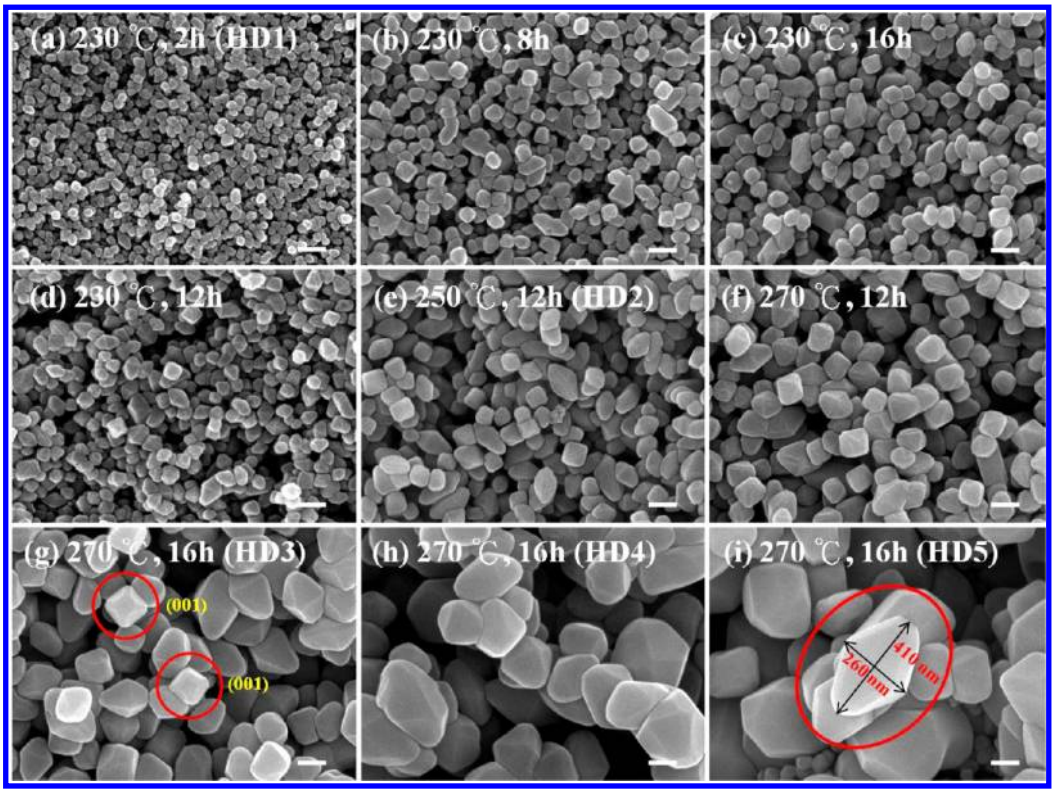

Figure 1. SEM images of TiO_2 nanocrystals in the HD series synthesized at varied hydrothermal conditions: (a) 230 °C and 2 h (HD1), (b) 230 °C and 8 h, (c) 230 °C and 16 h, (d) 230 °C and 12 h, (e) 250 °C and 12 h (HD2), (f) 270 °C and 12 h, (g) 270 °C and 16 h (HD3), (h) repeated hydrothermal treatment using the same sol with HD3 as a seed at 270 °C for 16 h (HD4); the red circles show the (001) facets. (i) Repeated hydrothermal treatment using the same sol with HD4 as a seed at 270 °C for 16 h (HD5); the red circle shows a titania single crystal with a truncated octahedral morphology of a extraordinarily large size. The scale bars indicate 100 nm for each plot.

crystals (HD5, Figure 1i) were formed; a typical HD5 single crystal highlighted in Figure 1i has diagonal size length of 410 nm and a width of 260 nm, which are appropriate for use as a SL for a DSSCs.

The formation of cuboidal TiO_2 nanocrystals was observed also in conventional sol−gel experiments at intermediate pH,[50,51] but the shape became altered from cuboidal to ellipsoidal under basic conditions (pH ~11.5),[50] in the presence of ammonia[52] or a primary, secondary, and tertiary amine.[51] Although the generation of octahedron-like TiO_2 nanocrystals is reported from a surfactant-assisted hydrothermal or solvothermal method under various experimental conditions,[15,18,42−47] the crystal sizes were small, <50 nm, even with autoclaving protracted up to 255 h.[42] From a solvothermal approach, for example, Wu *et al.*[46] reported the formation of monodisperse rhombic-shaped anatase titania single crystals of length ~20 nm using a primary amine as the capping agent. Dinh *et al.*[47] reported the shape-controlled synthesis of TiO_2 nanocrystals using oleic acid (OA) and oleylamine (OM) as distinct capping surfactants to generate rhombic and truncated rhombic anatase titania single crystals of length ~38 and ~18 nm, respectively; to suppress the growth of (101) facets, Yan *et al.*[15] synthesized octahedral anatase titania nanocrystals with ammonium bicarbonate as a surface-capping reagent and obtained nearly uniform TiO_2 nanooctahedra of size ~17 nm. A synthesis of octahedron-like anatase titania single crystals with a length as great as 400 nm that we achieved in the present work has never been reported elsewhere.

The detailed morphologies of HD1 are visible in the TEM and HRTEM images in Figure 2a,b, respectively. Consistent with the SEM images shown in Figure 1a, the TEM images of the HD1 crystals in Figure 2a exhibit mainly a "cuboidal" shape, but several crystals showing the octahedron-like shape are highlighted with red circles. The HRTEM image shown in Figure 2b indicates the distance between adjacent lattice fringes to be 0.35 nm, which matches exactly the lattice spacing of the (101) planes of anatase TiO_2.[12,15,44−47] The formation of purely crystalline nanocrystals HD1−HD5 in the anatase phase has been confirmed with the XRD patterns shown in Figure 3. The XRD signals increasingly sharpen from HD1 to HD5, indicating a greater crystallinity and a larger crystal. The three diffraction signals of the (103), (004), and (112) facets were well-resolved for the HD crystals, but those of the NP sample were congested and unresolved; this condition indicates that the HD crystals evolved along the [001] direction,[47] for which a mechanism of crystal growth is offered below. On the basis of this crystallographic

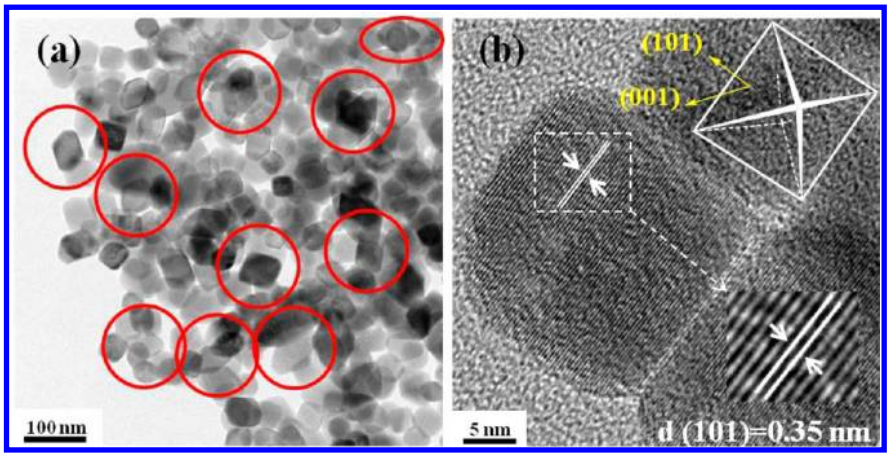

Figure 2. (a) TEM images of HD1 showing the cuboidal morphology of the nanocrystals; the red circles highlight the images with rhombic shapes that represent the formation of octahedron-like nanocrystals. (b) HRTEM image of one specific HD1 single crystal that can be emulated with a 3D octahedral structure with the directions of (101) and (001) planes as indicated; the inset shows the fine structure of the lattice with a distance of 0.35 nm between the (101) facets in the anatase phase.

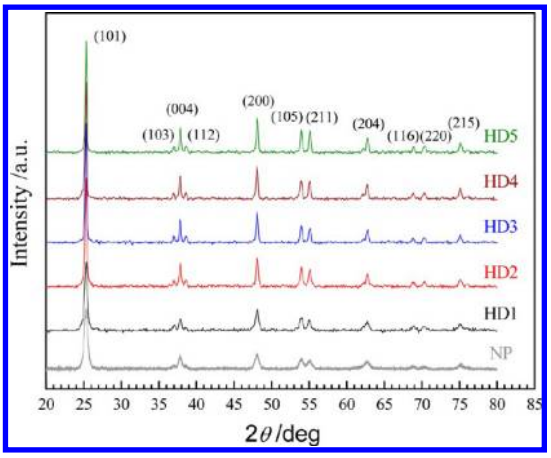

Figure 3. XRD patterns of base-catalyzed nanocrystals HD1–HD5 and acid-peptized nanoparticles (NP) exhibiting the well-defined signals assigned to the deflections of the lattice facets in the anatase phase (JCPDS no. 21-1272).

information, we constructed a speculative 3D octahedral geometry for a typical HD1 crystal shown in Figure 2b; the directions of both (101) and (001) facets are also indicated. According to the rhombic-shaped HRTEM images analyzed elsewhere,[15,44–47] we propose that the quadrate TEM image of HD1 shown in Figure 2b is the result of a projection from an octahedral crystal with a short *c*-axis, consistent with the observation of other crystals showing an octahedral geometry with a longer *c*-axis highlighted in Figure 2a.

Crystal Growth Mechanism. DEA served as a surface-capping agent in other sol–gel systems to promote the growth of ellipsoidal titania nanoparticles with small aspect ratios.[51,53] To examine the role of DEA played for the crystal growth in our system, we performed control experiments with the same synthetic procedure but without adding DEA in the third step of the sol preparation. We found that the crystal size, after hydrothermal treatment in the absence of DEA, is less than that in the presence of DEA at 230 °C for 2 h (Figure S1a, Supporting Information). Figure S1b, Supporting Information, shows that the crystal grew slowly at 270 °C for 16 h in the absence of DEA to attain a particle size of ~30 nm, which is much less than that of HD3 (Figure 1g) grown in the presence of DEA. DEA thus plays a key role not only as a catalyst to increase the rate of crystal growth but also as a shape controller to refine the nanocrystals with a beautiful truncated octahedral geometry. A mechanism for the crystal growth is presented in Scheme 1 to rationalize the formation of the octahedron-like anatase titania single crystals of extraordinary size.

In the first step, TEOA was mixed with TTIP at a molar ratio of 2:1; the solution turned from colorless to pale yellow, indicating the formation of a complex. We thus propose the formation of a TEOA-chelated titanium complex $[Ti(OR2)_n(OR1)_{4-2n}]$, with $n = 1$ or 2, of which the molecular structures of OR1 and OR2 are shown in Scheme 1. Sugimoto *et al.*[50–52] indicated that TEOA plays a role as a chelating agent to suppress rapid hydrolysis of the titanium complex. We treated TEOA as a bidentate ligand (OR2), but it might also act as a tridentate ligand.[54] When water was added to the mixture of TTIP and TEOA, hydration and hydrolysis occurred to form an octahedral complex, $[Ti(OH)_m(OR2)_n(H_2O)_{6-m-2n}]^{4-m-2n}$, with $m \leq 6$, $n \leq 3$, and $m + 2n \leq 6$. We expect that the bidentate ligand OR2 has a bridged chelating feature to prevent the approach of water molecules toward the central metal ion and thus may slow both the hydrolysis and the ensuing condensation.[55] For the sol–gel reaction performed at 100 °C for 24 h, we expect that the required hydrolysis and condensation generated a sol suitable for the subsequent hydrothermal reaction to proceed. As the titania nanocrystals were produced in only the pure anatase phase, the formation of $[Ti(OH)_2(H_2O)_4]^{2+}$ monomers is expected to generate nuclei of anatase type

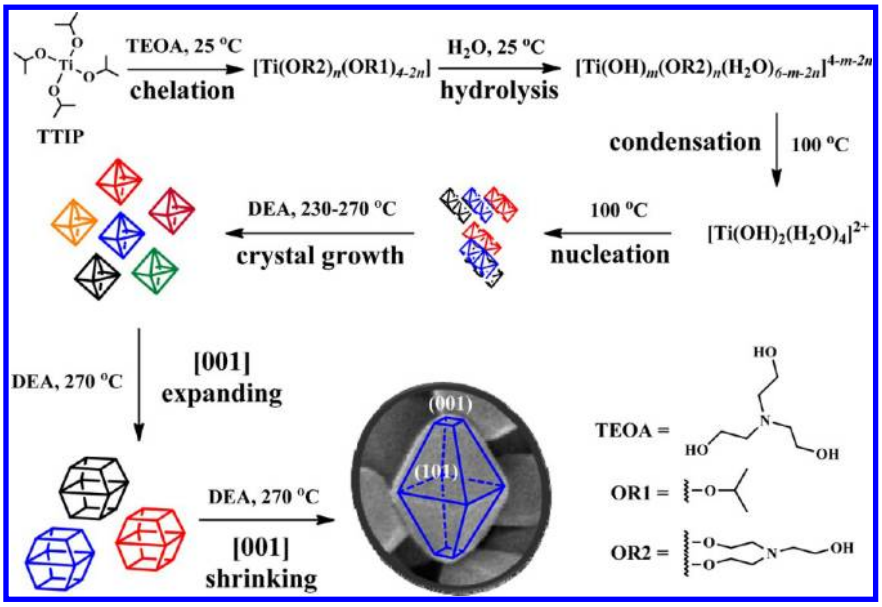

Scheme 1. Mechanism for the formation of anatase titania single crystals HD1−HD5 with octahedron-like morphology.

that serve as seeds in the solution for the succeeding condensation and nucleation.[56] Once nucleation generated the seed nuclei of anatase type, as the two crystal growth units shown in Scheme 1, DEA would play a key role as a bifunctional reagent—catalyst and shape controller—during the hydrothermal process to produce initially small octahedral (cuboid-like) nanocrystals (HD1), from which the crystals evolved to become large, truncated octahedral nanocrystals (HD3−HD5) as we have observed.

According to a mechanism involving a two-phase morphology evolution that Penn and Banfield proposed,[42] the growth of a crystal along the [001] facet is twice as rapid as that along the [101] facet in the first phase (hydrothermal duration 0−10 h), but it becomes 3−3.5 times as rapid along [001] than along [101] in the second phase (hydrothermal duration >10 h). The (001) faces hence expand during the first phase but shrink during the second phase. We observed that the crystal morphology evolved from an octahedral shape (HD1, Figure 2b) to a truncated octahedral shape with a larger exposed (001) facet (HD3, highlighted inside the red circles in Figure 1g), and then further evolved to a large truncated octahedron with a smaller exposed (001) facet (HD5, highlighted in Figure 1i). This evolution from HD1 to HD5 in our case can also be interpreted with a biphasic model, according to which the crystal growth along the [001] facet expanded from HD1 to HD3 and shrank from HD3 to HD5, as indicated in Scheme 1.

Why did such a (001) expanding and shrinking of the crystal evolution occur in our system? Dinh *et al.*[47] found that the evolution of the crystal shape depends on the molar ratio OA/OM, for which the rhombic, truncated rhombic, and spherical morphologies were produced at OA/OM ratios of 4/6, 5/5, and 6/4, respectively; only rhombic-type crystals were produced under more basic conditions (OA/OM < 4/6). It was proposed that the base OM tends to bind to the [101] facets, whereas the acid OA binds to the [001] facets to control the crystal growth in the corresponding directions. In our case, we expect that the base DEA plays a role similar to that of OM at 230 °C and hydrothermal period of 2 h to generate octahedral-type crystals of small size (HD1). At this stage, DEA functions as a surface-capping agent to inhibit the crystal growth along the [101] facets. When the temperature was increased to 270 °C for 16 h, the surface-capping effect gradually diminished because of the greatly enhanced surface area when the crystal was growing. At this stage, the catalytic role of DEA is expected to accelerate the crystal growth along the [101] facets to form truncated octahedral crystals of moderate size (HD3). TEOA released from the sol−gel reaction[50] might play a role similar to OA to inhibit the crystal growth along the (001) direction responsible for the formation of truncated octahedral crystals observed in this stage—a (001) expanding crystal evolution. When the crystals evolved further in the presence of a new sol solution, DEA in the fresh solution again played a role inhibiting the crystal growth along the (101) direction for the (001) shrinking to occur, producing the truncated octahedral crystals with a small exposed [001] area and an extraordinarily large size (HD5).

Photovoltaic Performance. Nanocrystals HD1−HD5 served as AL for DSSC applications; the devices were fabricated with identical components—N719 dye, iodide/triiodide electrolyte, and Pt counter electrode—except that TiO_2 AL was made of HD1−HD5 with the same film thickness (~11 μm). To assess the effect of these nanocrystals as AL on photovoltaic performance, we added no SL at this stage. The current−voltage

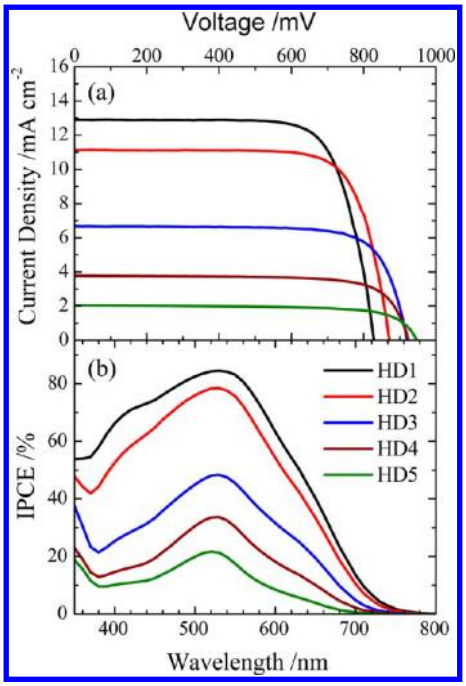

Figure 4. Optimized photovoltaic properties: (a) current−voltage characteristics and (b) corresponding IPCE action spectra of N719-dye-sensitized devices sensitized with TiO_2 active layers made of HD1−HD5 nanocrystals at a constant film thickness of ~11 μm without added scattering layer but with $TiCl_4$ post-treatment under irradiation (one-sun AM-1.5G).

(*J*−*V*) characteristics and the corresponding IPCE action spectra of these devices are shown in Figure 4a,b, respectively; the photovoltaic parameters are summarized in Table 1. Integrating the IPCE over the AM-1.5G solar spectrum (Figure S2, Supporting Information) yielded the calculated J_{SC} (shown in parentheses in Table 1), similar to the collected values for all devices under investigation, thus validating the photovoltaic results listed in Table 1 obtained from the *JV* measurement.

The photovoltaic performances of these devices exhibited a decreasing order of J_{SC} from HD1 to HD5, but V_{OC} showed an opposite trend, giving the best device HD1 with an efficiency η = 8.0% power conversion under a thin-film condition without an added SL. The systematic variation of J_{SC} is consistent with DL on the TiO_2 films, for which DL = 73 nmol cm^{-2} on film HD1, but it decreased to only 3 nmol cm^{-2} on film HD5. The specific surface areas (S_{BET}/m^2 g^{-1}) determined with the Brunauer−Emmett−Teller (BET) method gave values 62.7, 29.2, 13.0, 7.4, and 5.1 for HD1−HD5, respectively, which are consistent with the variation of DL showing the effect of particle size. The variation of V_{OC} is remarkable in that V_{OC} was significantly enhanced from 829 mV (HD1) to 949 mV (HD5), indicating the superior performance of HD5 nanocrystals of large size. Such a large V_{OC} in a DSSC based on an iodine electrolyte and with a N719 dye is unprecedented. We expect that the injected electrons in such a large single crystal would transport efficiently to the electrode, together with the small surface area to diminish the possibility of charge recombination for the observed appreciable V_{OC} of the HD5 device, but the large crystal size of HD5 leaves a small surface area available for dye adsorption, which leads to a small J_{SC} and a poor overall performance for the HD5 device.

TABLE 1. Amount of Dye Loading (DL), Specific Surface Area (S_{BET}), and Optimized Photovoltaic Parameters of Devices Made of N719 Dye and HD1−HD5 TiO_2 Films with Post-$TiCl_4$ Treatment under Simulated AM-1.5G Illumination (Power = 100 mW cm^{-2}) and Active Area of 0.16 cm^2 with a Shadow Mask Area of 0.25 cm^2[a]

TiO_2 film	DL (nmol cm^{-2})	S_{BET} (m^2 g^{-1})	J_{SC}[b] (mA cm^{-2})	V_{OC} (mV)	FF	η (%)
HD1	73	62.7	12.89 (12.78)	829	0.747	8.0
HD2	33	29.2	11.15 (11.13)	873	0.753	7.3
HD3	15	13.0	6.68 (6.32)	922	0.747	4.6
HD4	7.4	7.4	3.77 (3.87)	927	0.747	2.6
HD5	2.8	5.1	2.06 (2.22)	949	0.714	1.4

[a] The devices contain only one active layer of the same film thickness (~11 μm) without added scattering layer. [b] The values shown in parentheses were obtained from integration of the IPCE spectra with the solar irradiance flux spectra.

According to the marked performance of HD1 at a thin-film condition, we further tested the effect of film thickness on device performance using HD1 as AL and HD5 as SL. As a reference for comparison, the experiments were also performed with NP as AL and CCIC as SL according to the same procedure as that of Ito *et al.*[40] For the HD1 + HD5 system, the total thickness (*L*) of the AL + SL film was readily controllable across a broad range from 17 to 32 μm; for the NP + CCIC system, a thick film tended to crack, which limited the film thickness to a range of 15−22 μm. In both cases, the thickness of the SL was fixed at ~5 μm. The *JV* curves obtained for the HD1 + HD5 system (six devices) and the NP + CCIC system (four devices) are shown in Figure S3a,b, respectively; the corresponding DL and photovoltaic parameters are summarized in Table S1, Supporting Information.

Figure 5a−e shows parameters DL, J_{SC}, V_{OC}, FF, and η as a function of *L*, respectively. The results indicate that DL increased as *L* increased for both systems, consistent with the variation of J_{SC} for the HD system to attain the maximum J_{SC} value, 16.27 mA cm^{-2}, at *L* = 32 μm. For the NP system, J_{SC} attained its maximum value, 16.18 mA cm^{-2}, at *L* = 20 μm, in agreement with the results of Ito *et al.* that show the best performance of a device to occur at *L* = 17−19 μm (12−14 μm for AL).[40] The DL values are much greater for NP than for HD at similar *L* because the particle size of NP was much smaller than that of HD, making the surface area of the former much greater than that of the latter. Larger amounts of loaded dye increased J_{SC} for the NP devices to outperform the HD devices for *L* < 21 μm, but the robust mechanical structure of the HD films enabled us to make thicker films to enhance DL and J_{SC}

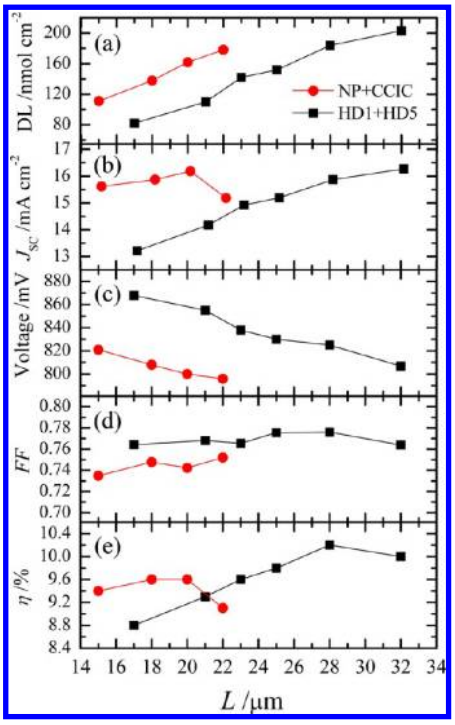

Figure 5. (a) Amounts of dye loading (DL) and DSSC photovoltaic parameters, (b) short-circuit current density (J_{SC}), (c) open-circuit voltage (V_{OC}), (d) fill factor (FF), and (e) efficiency (η) of power conversion, as a function of total TiO_2 film thickness (L). The results were obtained from the HD1 + HD5 system (filled squares) and the NP + CCIC system (filled circles) for which HD1 or NP served as an active layer (AL) and HD5 or CCIC served as a scattering layer (SL). The thickness of the SL was fixed at ~5 μm for all devices.

for the HD devices, to outperform the NP devices for $L > 21$ μm.

The trend of V_{OC} is opposite that of J_{SC} because charge recombination plays a key role in film thickness (discussed in the next section). Upon increasing L for both systems, the V_{OC} values decreased linearly and in parallel with ~50 mV advance for the HD over the NP system. The FF values show no correlation with L, but the average value of HD is slightly greater than that of NP, which might indicate the advantage of HD films with conductivity greater than that of NP films. Because of the countertendency between V_{OC} and J_{SC}, upon increasing the film thickness, the overall performance of the HD devices was dominated by J_{SC} until a maximum efficiency was attained at $L = 28$ μm, for which $J_{SC} = 15.87$ mA cm^{-2}, $V_{OC} = 825$ mV, FF = 0.776, and $\eta = 10.2\%$. For the NP devices, the best performance ($\eta = 9.6\%$) occurred for $L = 18-20$ μm.

Arakawa and co-workers[19] tested film composition with varied particle size on device performance as a function of film thickness; when they varied the film thickness of a mixed particle system (particle sizes of 23 and 100 nm) in a broad range (11−31 μm), they found an optimal thickness in the range of 15−18 μm; both J_{SC} and V_{OC} decreased for a film thicker than 18 μm. To test the effect of film thickness on device performance, Adachi and co-workers[13] used TiO_2 films composed of highly crystalline nanorods with a length of 100−300 nm and a diameter of 20−30 nm; the optimal performance of the nanorod cell occurred at a film thickness greater than 16 μm, whereas the P25 cell attained the best performance at a smaller thickness; that the FF values were greater for the nanorod devices than for the P25 devices was attributed to the high crystallinity of the nanorod films. In our system, the best performance of the HD devices occurred at an overall film thickness of 23 + 5 μm, which is difficult to attain for a regular DSSC system but is feasible in our HD1 + HD5 system because of the remarkable mechanical strength of the films; in that manner, an enhanced DL can be achieved to overcome the shortage of HD1 single crystals with a small specific surface area.

Transient Photoelectric Measurements. To understand the discrepancy of the device performance between the two systems, we fabricated three devices, HD-18, HD-29, and NP-17, for transient photoelectric measurements. The HD-18 and HD-29 devices are based on the HD1 + HD5 system with the total film thicknesses of 18 and 29 μm, respectively; the NP-17 device is based on the NP + CCIC system with a total film thickness of 17 μm. All three devices involve a SL of the same film thickness, ~5 μm. The corresponding *JV* curves and IPCE action spectra of these three devices are shown in Figure S4a,b, respectively. The kinetics of electron transport and charge recombination of these devices were investigated *via* decays of ΔJ_{SC} and ΔV_{OC} *versus* time, respectively, based on eight white-light (WL) intensities as bias irradiations (power densities P_0 in a range of 4.2−98 mW cm^{-2}). The photoelectric transients were obtained with a red pulsed LED ($\lambda = 630$ nm, duration ~50 ms) under these WL bias irradiations; the resulting photocurrent and photovoltage decays are shown in Figures S5−S10, Supporting Information.

Decay curves of ΔJ_{SC} and ΔV_{OC} *versus* time of these devices were fitted according to a single exponential function to determine time coefficients for electron collection (τ_C) and charge recombination (τ_R), respectively. For the kinetics of electron transport, we show τ_C and diffusion coefficients (D) as a function of J_{SC} in Figure 6a,b, respectively. Our results indicate that the electron collection periods of the NP-17 and HD-29 devices are similar but much greater than those of the HD-18 device when compared at the same J_{SC} level. The large τ_C values of the HD-29 device are due to its thicker film, for which greater durations of transport are required to collect the electrons at the TCO electrode. When the film thickness is taken into account, the collection periods become convertible into diffusion coefficients *via* $D = L^2/(2.77\tau_C)$.[57] As shown in Figure 6b, the diffusion coefficients of both HD-18 and HD-29 devices are similar to each other but are 3 times those of the NP-17 device, indicating that the

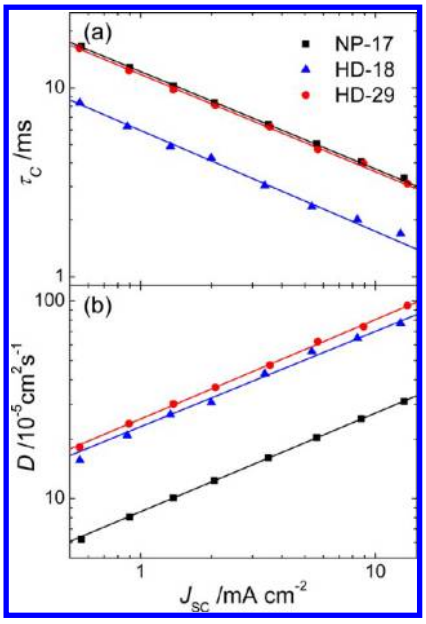

Figure 6. (a) Electron collection period (τ_C) and (b) electron diffusion coefficient (D) as a function of short-circuit current density (J_{SC}) generated under eight bias white-light irradiations for NP-17, HD-18, and HD-29 devices. HD and NP represent devices fabricated based on HD1 + HD5 and NP + CCIC films, respectively, with the suffixed numeric labels representing the total film thickness (L).

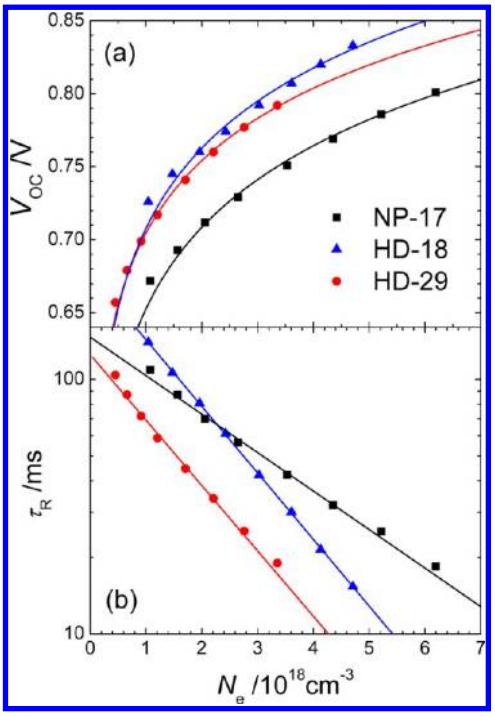

Figure 7. (a) Open-circuit voltage (V_{OC}) and (b) electron lifetime (τ_R) as a function of charge density (N_e) generated under eight bias white-light irradiations for NP-17, HD-18, and HD-29 devices. HD and NP represent the devices fabricated based on HD1 + HD5 and NP + CCIC films, respectively, with suffixed numeric labels representing total film thickness (L).

electron transport of the HD nanocrystals is much superior to that of the NP nanoparticles as an AL for DSSCs.[58]

To make a fair comparison of charge recombination kinetics of the systems under investigation, we examined the location of the edge of the conduction band of TiO_2 with a charge-extraction method. For this purpose, charge densities (N_e) at each V_{OC} were extracted *via* rapid switching of the three devices to the short-circuit condition.[57] Figure 7a,b shows plots of V_{OC} and τ_R as a function of N_e, respectively. The results in Figure 7a indicate that the TiO_2 potentials of the two HD films are similar, with the edge of the potential band of thinner film HD-18 being slightly greater than that of thicker film HD-29, but the potentials of both HD films are located significantly above the potential of the NP film. The potential shift by ~50 mV between the HD-18 and the NP-17 films is consistent with discrepancy of V_{OC} showing a ~30 mV advance for the HD devices over the NP devices (Figure S4a). Figure 7b shows that the electron lifetimes of the HD-29 device are much smaller than those of the HD-18 device compared at the same charge density, indicating that charge recombination was more significant in the thicker film than in the thinner film, so that the V_{OC} decreased upon increasing the film thickness, as shown in Figure 5c and Figures S3 and S4a. Both HD and NP systems were compared at a similar film thickness (HD-18 *vs* NP-17): the electron lifetimes of HD-18 were larger than those of NP-17 at smaller charge densities, but the trend reversed at greater charge densities. We expect that the larger surface area of the NP film and greater DL retard charge recombination more efficiently than for the HD film at a larger N_e, but the electrons inside HD nanocrystals transported more rapidly than inside the NP nanoparticles: the electrons trapped at the surface of the HD-18 device become fewer than for the NP-17 device, so that charge recombination is prevented more effectively for the former than the latter at a smaller N_e. As the electron lifetimes of both HD-18 and NP-17 have the same order of magnitude, we believe that the discrepancy of V_{OC} is due mainly to the difference of the edge of the potential band between the two systems as we observed according to the measurements of charge extraction.[59]

CONCLUSION

Octahedron-like anatase TiO_2 single crystals, HD1–HD5, with particle sizes in a range of 30–400 nm were prepared according to a simple two-step sol/hydrothermal approach: the first step prepared a suitable TTIP/TEOA/DEA sol at a basic condition (pH 9.6); the second step involved a hydrothermal treatment of varied temperature (230–270 °C) and duration (2–16 h). At autoclave temperature of 230 °C for a period of 2 h, cuboid-like and octahedron-like nanocrystals of size ~30 nm (HD1) were produced. At hydrothermal temperature of 270 °C for 16 h, the crystals evolved to a

truncated octahedral morphology with a length of ~150 nm and a width of ~100 nm (HD3). Performing the same hydrothermal treatment (270 °C for 16 h) with HD3 as a seed with a fresh TTIP/TEOA/DEA sol, larger octahedral single crystals (HD4) evolved. Repeating the same experiment with HD4 as a seed, extraordinarily large octahedral anatase titania single crystals (HD5) were generated, of a typical length of 410 nm and width of 260 nm. Base diethylamine (DEA) played a bifunctional role as both a catalyst and controller of shape for the crystal growth; on that basis, we proposed a biphasic mechanism of crystal evolution. When HD1−HD5 served as active layers for dye-sensitized solar cells with N719 dye as a photosensitizer, the photovoltaic performances exhibited a systematic trend with J_{SC} decreasing from HD1 to HD5, consistent with their dye-loading amounts reflecting their specific surface areas. In contrast, V_{OC} showed an increasing order from HD1 to HD5; the best value attained 0.949 V for HD5. Among these devices, HD1 was the best candidate as an active layer to attain η = 8.0% with the film thickness fixed at ~11 μm. The device performance of HD1 was further optimized to attain η = 10.2% at a film thickness of ~23 μm together with HD5 at ~5 μm as a light-scattering layer; that result is superior to that, η = 9.6%, of a conventional nanoparticle-type DSSC (NP + CCIC) optimized at a total film thickness of 18−20 μm (CCIC ~5 μm). To understand the electron transport and charge recombination kinetics of these devices, we performed transient photoelectric and charge-extraction measurements. The outstanding performance of the HD devices relative to the NP devices is attributed to the greater rate of electron transport and the more negative potential for the HD than for the NP system, making the HD single crystals a promising photoanode material for further promotion of device performance for other sensitizers and co-sensitization systems.

EXPERIMENTAL DETAILS

Preparation of Base-Catalyzed TiO_2 Nanocrystals (HD1−HD5). The experimental procedures are summarized in Scheme S1, Supporting Information; the details are given below. Of three steps to make the required sol, in the first, TTIP (0.1 mol, 29.3 mL, 97%; Aldrich) was slowly added to a beaker containing TEOA (0.2 mol, 26.6 mL, 95+%; TEDIA) and stirred for 5 min at 25 °C; the color of the TTIP/TEOA (1/2) mixture turned pale yellow, which indicated the formation of a TEOA-chelated titanium complex. In the second step, water (100 mL) was added to the beaker to form the TTIP/TEOA aqueous solution and stirred for 6 h at 25 °C; the color of the solution became transparently light yellow. In the third step, DEA (0.02 mol, 2.1 mL, 99+%; ACROS) and water (100 mL) were added to the TTIP/TEOA aqueous solution and then stirred 24 h at 100 °C, resulting in the formation of a translucent solution; the prepared TTIP/TEOA/DEA sol was thus ready for the following hydrothermal reaction.

For the hydrothermal synthesis of HD1−HD5, the TTIP/TEOA/DEA sol was transferred into a titanium autoclave and kept at a constant temperature in a range of 230−270 °C (autoclave pressure 40−60 bar) for a duration of 2−16 h. For example, the HD1 nanocrystals were obtained at 230 °C for 2 h, HD2 at 250 °C for 12 h, and HD3 at 270 °C for 16 h. For HD4, we used HD3 as seed crystals and mixed them with the same sol already prepared for hydrothermal reaction at 270 °C for 16 h; for HD5, with HD4 as seed crystals, the procedure was repeated as for HD4. These HD particles were then collected on centrifugation and washed several times with ethanol. To prepare a screen-printable paste, ethyl cellulose and α-terpineol were added to the ethanol solution of the TiO_2 nanocrystals HD1−HD5; ethanol was then removed from the solution with a rotary evaporator to obtain a viscous paste suitable for screen printing.[60]

Preparation of Acid-Peptized TiO_2 Nanoparticles (NP). The anatase TiO_2 nanoparticles (NP) under acidic conditions were prepared according to a conventional synthetic procedure reported by Grätzel and co-workers,[3,40] but with a minor modification; the detailed procedure follows. First, TTIP (0.06 mol, 17.7 mL) was added to a flask containing ethanoic acid (0.06 mol, 3.4 mL, glacial; J.T. Baker) and stirred for 15 min at 25 °C; a white precipitate was formed at this stage. Second, water (100 mL) was added slowly to the beaker and stirred for 1 h at 25 °C; the produced white turbid solution indicates that the hydrolysis of the sol led to a solution of gel-type solution. Third, nitric acid (0.03 mol, 1.3 mL, 70%; J.T. Baker) was poured into the flask containing the gel-type aqueous solution and heated to 80 °C while the solution was continuously stirred for 1 h; nitric acid served as peptizer for the sol−gel reaction, and the solution appeared foggy in this stage. After peptization, the gel-type solution was transferred into a titanium autoclave and heated to 230 °C for total autoclave period of 12 h to complete the hydrothermal process. The NP particles were eventually collected on centrifugation, washed several times with ethanol, and then prepared as the required paste for screen printing according to a procedure reported elsewhere.[60]

Characterization of Morphology. The morphology of the TiO_2 samples was investigated with a field-emission scanning electron microscope (FESEM, JSM-7401F, JEOL). The microstructures of the products were analyzed with a high-resolution transmission electron microscope (FE-HRTEM, JEM-2100F, JEOL) with energy-dispersive X-ray (EDX) analysis of the composition. The crystal phases of the products were characterized with an X-ray diffractometer (XRD, X'Pert Pro, PANalytical, Cu Kα radiation), in a 2θ range from 10 to 80°. The specific surface area and porosity of the TiO_2 nanocrystals were determined with a nitrogen adsorption−desorption apparatus (model TriStar 3000 and VacPrep 061, Micromeretics).

Fabrication of DSSCs. For the working electrode, a paste composed of TiO_2 HD1−HD5 or NP as a transparent AL was coated on a $TiCl_4$-treated FTO glass substrate (TEC 7, Hartford, USA) to obtain a film of the required thickness (active size 0.4 × 0.4 cm^2) with repetitive screen printing. Both our HD5 and the commercially available CCIC (PST-400C, JGC Catalysts and Chemicals Ltd., Japan) served as the SL to print on top of the transparent nanocrystalline TiO_2 AL with a film thickness of ~5 μm. The TiO_2 films were annealed according to a programmed procedure: heating at 80 °C for 15 min, at 135 °C for 10 min, at 325 °C for 30 min, at 375 °C for 5 min, at 450 °C for 15 min, and at 500 °C for 15 min. The annealed films were then treated with $TiCl_4$ fresh aqueous solution (40 mM) at 70 °C for 30 min and sintered at 500 °C for 30 min. The TiO_2 films as prepared were sensitized in a solution (N719 dye, Solaronix, 3×10^{-4} M) containing chenodeoxycholic acid (CDCA, 3×10^{-4} M) in acetonitrile/*tert*-butanol mixture (v/v = 1:1) for 18 h. The electrolyte solution containing GuNCS (0.1 M), I_2 (0.03 M), PMII (0.6 M), 4-*tert*-butylpyridine (0.5 M) in a mixture of acetonitrile and valeronitrile (volume ratio 85:15) was introduced into the space between the two electrodes, completing the fabrication of these DSSC devices.

Photovoltaic Characterization. The photovoltaic performance of a device was assessed through measurement of a *J*−*V* curve with a solar simulator (AM-1.5G, XES-40S1, SAN-EI), calibrated

with a standard Si reference cell (Oriel PN 91150 V, VLSI standards). The efficiency (η) of conversion of light to electricity was obtained *via* $\eta = J_{SC}V_{OC}FF/P_{in}$, in which J_{SC}/mA cm^{-2} is the current density measured at short circuit and V_{OC}/V is the voltage measured at open circuit. P_{in} is the input radiation power (for one-sun illumination P_{in} = 100 mW cm^{-2}), and FF is the fill factor. For all measurements, the DSSC devices were covered with a black mask (aperture area 0.25 cm^2) to ensure that the measured photocurrent was not exaggerated. The incident monochromatic efficiencies for conversion from photons to current (IPCE) spectra of the corresponding devices were measured with a system comprising a Xe lamp (A-1010, PTi, 150 W), monochromator (PTi, 1200 gr mm^{-1} blazed at 500 nm), and source meter (Keithley 2400, computer-controlled). A standard Si photodiode (S1337-1012BQ, Hamamatsu) served as a reference for the calibration of the power density of the lamp at each wavelength.

Transient Photoelectric Characterization. The photocurrent and photovoltage decays were measured with eight steady-state light intensities as bias irradiations from a white LED.[57] A red LED (λ = 630 nm) controlled with a pulse generator (DG535, SRS) generated a perturbation pulse of duration 50 ms. Both the pulsed red light and the steady-state white light irradiated the photoanode side of the cell. The pulsed-probe irradiation was controlled with a LED power supply to maintain the modulated photovoltage less than 5 mV in each measurement. The probe beams generated carriers causing a slightly increased photocurrent (ΔJ_{SC}) near J_{SC} of the cell at the short-circuit condition or a slightly increased photovoltage (ΔV_{OC}) near V_{OC} of the cell at the open-circuit condition, subjected to the white bias light; the current and voltage decays were thereby measured, respectively. The resulting photocurrent and photovoltage transients were recorded on a digital oscilloscope (MSO2014, Tektronix); the signals passed a current preamplifier (SR570, SRS) at a short-circuit condition.

Measurement of Charge Extraction. The extracted charges were measured with the same apparatus as that of the transient photoelectric measurements, but with only the white LED at eight intensities of bias light.[57] Under white LED irradiation, the system was initially set to an open-circuit condition for about 200−300 ms for the photovoltage of the device to attain a steady state; the white LED was then terminated while the device was simultaneously switched to a short-circuit condition with a rapid electronic switch controlled with a pulse generator (DG535, SRS). The transient signals of voltage across 50 Ω were concurrently recorded with a digital oscilloscope (MSO2014, Tektronix) and converted into current transients with Ohm's law. The extracted charge (Q_{CE}) was obtained on integration of the current transient *versus* time; the extracted charge density (N_e) is determined with the equation, $N_e = (Q_{CE})/(eL(1-p))$, in which e is elementary charge, L is the thickness of the TiO_2 film, and p is the porosity of TiO_2.

Conflict of Interest: The authors declare no competing financial interest.

Acknowledgment. National Science Council of Taiwan and Ministry of Education of Taiwan, under the ATU program, provided support for this project.

Supporting Information Available: Schematic illustration of the synthesis of HD1−HD5 TiO_2 single crystals, additional SEM images for the crystals synthesized in the absence of DEA, supplementary table and figures for photovoltaic and transient photoelectric data. This material is available free of charge *via* the Internet at http://pubs.acs.org.

REFERENCES AND NOTES

1. Chen, X.; Mao, S. S. Titanium Dioxide Nanomaterials: Synthesis, Properties, Modifications, and Applications. *Chem. Rev.* **2007**, *107*, 2891–2959.
2. Khataee, A.; Mansoori, G. A. *Nanostructured Titanium Dioxide Materials: Properties, Preparation and Applications*; World Scientific: Singapore, 2012.
3. Barbé, C. J.; Arendse, F.; Comte, P.; Jirousek, M.; Lenzmann, F.; Shklover, V.; Grätzel, M. Nanocrystalline Titanium Oxide Electrodes for Photovoltaic Applications. *J. Am. Ceram. Soc.* **1997**, *80*, 3157–3171.
4. Grätzel, M. Photoelectrochemical Cells. *Nature* **2001**, *414*, 338–344.
5. Grätzel, M. Recent Advances in Sensitized Mesoscopic Solar Cells. *Acc. Chem. Res.* **2009**, *42*, 1788–1798.
6. Hagfeldt, A.; Boschloo, G.; Sun, L.; Kloo, L.; Pettersson, H. Dye-Sensitized Solar Cells. *Chem. Rev.* **2010**, *110*, 6595–6663.
7. Koo, H.-J.; Park, J.; Yoo, B.; Yoo, K.; Kim, K.; Park, N.-G. Size-Dependent Scattering Efficiency in Dye-Sensitized Solar Cell. *Inorg. Chem. Acta* **2008**, *361*, 677–683.
8. Yu, I. G.; Kim, Y. J.; Kim, H. J.; Lee, C.; Lee, W. I. Size-Dependent Light-Scattering Effects of Nanoporous TiO_2 Spheres in Dye-Sensitized Solar Cells. *J. Mater. Chem.* **2011**, *21*, 532–538.
9. Park, Y.-C.; Chang, Y.-J.; Kum, B.-G.; Kong, E.-H.; Son, J. Y.; Kwon, Y. S.; Park, T.; Jang, H. M. Size-Tunable Mesoporous Spherical TiO_2 as a Scattering Overlayer in High-Performance Dye-Sensitized Solar Cells. *J. Mater. Chem.* **2011**, *21*, 9582–9586.
10. Kim, Y. J.; Lee, M. H.; Kim, H. J.; Lim, G.; Choi, Y. S.; Park, N.-G.; Kim, K.; Lee, W. I. Formation of Highly Efficient Dye-Sensitized Solar Cells by Hierarchical Pore Generation with Nanoporous TiO_2 Spheres. *Adv. Mater.* **2009**, *21*, 3668–3673.
11. Chen, Y.; Huang, F.; Chen, D.; Cao, L.; Zhang, X. L.; Caruso, R. A.; Cheng, Y.-B. Effect of Mesoporous TiO_2 Bead Diameter in Working Electrodes on the Efficiency of Dye-Sensitized Solar Cells. *ChemSusChem* **2011**, *4*, 1498–1503.
12. Adachi, M.; Murata, Y.; Takao, J.; Jiu, J.; Sakamoto, M.; Wang, F. Highly Efficient Dye-Sensitized Solar Cells with a Titania Thin-Film Electrode Composed of a Network Structure of Single-Crystal-Like TiO_2 Nanowires Made by the "Oriented Attachment" Mechanism. *J. Am. Chem. Soc.* **2004**, *126*, 14943–14949.
13. Jiu, J.; Isoda, S.; Wang, F.; Adachi, M. Dye-Sensitized Solar Cells Based on a Single-Crystalline TiO_2 Nanorod Film. *J. Phys. Chem. B* **2006**, *110*, 2087–2092.
14. Fujihara, K.; Kumar, A.; Jose, R.; Ramakrishna, S.; Uchida, S. Spray Deposition of Electrospun TiO_2 Nanorods for Dye-Sensitized Solar Cell. *Nanotechnology* **2007**, *18*, 365709.
15. Yan, K.; Qiu, Y.; Chen, W.; Zhang, M.; Yang, S. A Double Layered Photoanode Made of Highly Crystalline TiO_2 Nanooctahedra and Agglutinated Mesoporous TiO_2 Microspheres for High Efficiency Dye Sensitized Solar Cells. *Energy Environ. Sci.* **2011**, *4*, 2168–2176.
16. Zhang, H.; Han, Y.; Liu, X.; Liu, P.; Yu, H.; Zhang, S.; Yao, X.; Zhao, H. Anatase TiO_2 Microspheres with Exposed Mirror-like Plane {001} Facets for High Performance Dye-Sensitized Solar Cells. *Chem. Commun.* **2010**, *46*, 8395–8397.
17. Yang, W.; Li, J.; Wang, Y.; Zhu, F.; Shi, W.; Wan, F.; Xu, D. A Facile Synthesis of Anatase TiO_2 Nanosheets-Based Hierarchical Spheres with over 90% {001} Facets for Dye-Sensitized Solar Cells. *Chem. Commum.* **2011**, *47*, 1809–1811.
18. Wu, X.; Chen, Z. G.; Lu, G. Q.; Wang, L. Z. Nanosized Anatase TiO_2 Single Crystals with Tunable Exposed (001) Facets for Enhanced Energy Conversion Efficiency of Dye-Sensitized Solar Cells. *Adv. Funct. Mater.* **2011**, *21*, 4167–4172.
19. Wang, Z.-S.; Kawauchi, H.; Kashima, T.; Arakawa, H. Significant Influence of TiO_2 Photoelectrode Morphology on the Energy Conversion Efficiency of N719 Dye-Sensitized Solar Cell. *Coord. Chem. Rev.* **2004**, *248*, 1381–1389.
20. Dürr, M.; Schmid, A.; Obermaier, M.; Rosselli, S.; Yasuda, A.; Nelles, G. Low-Temperature Fabrication of Dye-Sensitized Solar Cells by Transfer of Composite Porous Layers. *Nat. Mater.* **2005**, *4*, 607–611.
21. Hore, S.; Nitz, P.; Vetter, C.; Prahl, C.; Niggemann, M.; Kern, R. Scattering Spherical Voids in Nanocrystalline TiO_2-Enhancement of Efficiency in Dye-Sensitized Solar Cells. *Chem. Commun.* **2005**, 2011–2013.
22. Koo, H.-J.; Kim, Y. J.; Lee, Y. H.; Lee, W. I.; Kim, K.; Park, N.-G. Nano-Embossed Hollow Spherical TiO_2 as Bifunctional

Material for High-Efficiency Dye-Sensitized Solar Cells. *Adv. Mater.* **2008**, *20*, 195–199.
23. Han, S.-H.; Lee, S.; Shin, H.; Jung, H. S. A Quasi-Inverse Opal Layer Based on Highly Crystalline TiO_2 Nanoparticles: A New Light-Scattering Layer in Dye-Sensitized Solar Cells. *Adv. Energy Mater.* **2011**, *1*, 546–550.
24. Liao, J.-Y.; Lei, B.-X.; Kuang, D.-B.; Su, C.-Y. Tri-functional Hierarchical TiO_2 Spheres Consisting of Anatase Nanorods and Nanoparticles for High Efficiency Dye-Sensitized Solar Cells. *Energy Environ. Sci.* **2011**, *4*, 4079–4085.
25. Chen, D.; Huang, F.; Cheng, Y.-B.; Caruso, R. A. Mesoporous Anatase TiO_2 Beads with High Surface Areas and Controllable Pore Sizes: A Superior Candidate for High-Performance Dye-Sensitized Solar Cells. *Adv. Mater.* **2009**, *21*, 2206–2210.
26. Huang, F.; Chen, D.; Zhang, X. L.; Caruso, R. A.; Cheng, Y.-B. Dual-Function Scattering Layer of Submicrometer-Sized Mesoporous TiO_2 Beads for High-Efficiency Dye-Sensitized Solar Cells. *Adv. Funct. Mater.* **2010**, *20*, 1301–1305.
27. Sauvage, F.; Chen, D.; Comte, P.; Huang, F.; Heiniger, L.-P.; Cheng, Y.-B.; Caruso, R. A.; Gräetzel, M. Dye-Sensitized Solar Cells Employing a Single Film of Mesoporous TiO_2 Beads Achieve Power Conversion Efficiencies over 10%. *ACS Nano* **2010**, *4*, 4420–4425.
28. Ghadiri, E.; Taghavinia, N.; Zakeeruddin, S. M.; Grätzel, M.; Moser, J.-E. Enhanced Electron Collection Efficiency in Dye-Sensitized Solar Cells Based on Nanostructured TiO_2 Hollow Fibers. *Nano Lett.* **2010**, *10*, 1632–1638.
29. Hwang, K.-J.; Cho, D. W.; Lee, J.-W.; Im, C. Preparation of Nanoporous TiO_2 Electrodes Using Different Mesostructured Silica Templates and Improvement of the Photovoltaic Properties of DSSCs. *New J. Chem.* **2012**, *36*, 2096–2100.
30. Chen, C.-C.; Chung, H.-W.; Chen, C.-H.; Lu, H.-P.; Lan, C.-M.; Chen, S.-F.; Luo, L.-Y.; Hung, C.-S.; Diau, E. W.-G. Fabrication and Characterization of Anodic Titanium Oxide Nanotube Arrays of Controlled Length for Highly Efficient Dye-Sensitized Solar Cells. *J. Phys. Chem. C* **2008**, *112*, 19151–19157.
31. Li, L.-L.; Tsai, C.-Y.; Wu, H.-P.; Chen, C.-C.; Diau, E. W.-G. Fabrication of Long TiO_2 Nanotube Arrays in a Short Time Using a Hybrid Anodic Method for Highly Efficient Dye-Sensitized Solar Cells. *J. Mater. Chem.* **2010**, *20*, 2753–2758.
32. Li, L.-L.; Chen, Y.-J.; Wu, H.-P.; Wang, N. S.; Diau, E. W.-G. Detachment and Transfer of Ordered TiO_2 Nanotube Arrays for Front-Illuminated Dye-Sensitized Solar Cells. *Energy Environ. Sci.* **2011**, *4*, 3420–3425.
33. Enache-Pommer, E.; Liu, B.; Aydil, E. S. Electron Transport and Recombination in Dye-Sensitized Solar Cells Made from Single-Crystal Rutile TiO_2 Nanowires. *Phys. Chem. Chem. Phys.* **2009**, *11*, 9648–9652.
34. Zhang, H.; Yu, H.; Han, Y.; Liu, P.; Zhang, S.; Wang, P.; Cheng, Y.; Zhao, H. Rutile TiO_2 Microspheres with Exposed Nano-Acicular Single Crystals for Dye-Sensitized Solar Cells. *Nano Res.* **2011**, *4*, 938–947.
35. Sheng, J.; Hu, L.; Li, W.; Mo, L.; Tian, H.; Dai, S. Formation of Single-Crystalline Rutile TiO_2 Splitting Microspheres for Dye-Sensitized Solar Cells. *Sol. Energy* **2011**, *85*, 2697–2703.
36. Hore, S.; Palomares, E.; Smit, H.; Bakker, N. J.; Comte, P.; Liska, P.; Thampi, K. R.; Kroon, J. M.; Hinsch, A.; Durrant, J. R. Acid *versus* Base Peptization of Mesoporous Nanocrystalline TiO_2 Films: Functional Studies in Dye Sensitized Solar Cells. *J. Mater. Chem.* **2005**, *15*, 412–418.
37. Nazeeruddin, M. K.; Kay, A.; Rodicio, I.; Humphry-Baker, R.; Müller, E.; Liska, P.; Vlachopoulos, N.; Grätzel, M. Conversion of Light to Electricity by *cis*-X2bis(2,2′-bipyridyl-4,4′-dicarboxylate)ruthenium(II) Charge-Transfer Sensitizers (X = Cl^-, Br^-, I^-, CN^-, and SCN^-) on Nanocrystalline Titanium Dioxide Electrodes. *J. Am. Chem. Soc.* **1993**, *115*, 6382–6390.
38. Nazeeruddin, M. K.; De Angelis, F.; Fantacci, S.; Selloni, A.; Viscardi, G.; Liska, P.; Ito, S.; Takeru, B.; Grätzel, M. Combined Experimental and DFT-TDDFT Computational Study of Photoelectrochemical Cell Ruthenium Sensitizers. *J. Am. Chem. Soc.* **2005**, *127*, 16835–16847.
39. Wang, Q.; Ito, S.; Grätzel, M.; Fabregat-Santiago, F.; Mora-Seró, I.; Bisquert, J.; Bessho, T.; Imai, H. Characteristics of High Efficiency Dye-Sensitized Solar Cells. *J. Phys. Chem. B* **2006**, *110*, 25210–25221.
40. Ito, S.; Murakami, T. N.; Comte, P.; Liska, P.; Grätzel, C.; Nazeeruddin, M. K.; Grätzel, M. Fabrication of Thin Film Dye Sensitized Solar Cells with Solar to Electric Power Conversion Efficiency over 10%. *Thin Solid Films* **2008**, *516*, 4613–4619.
41. Burnside, S. D.; Shklover, V.; Barbé, C.; Comte, P.; Arendse, F.; Brooks, K.; Grätzel, M. Self-Organization of TiO_2 Nanoparticles in Thin Films. *Chem. Mater.* **1998**, *10*, 2419–2425.
42. Penn, R. L.; Banfield, J. F. Morphology Development and Crystal Growth in Nanocrystalline Aggregates under Hydrothermal Conditions: Insights from Titania. *Cosmochim. Acta* **1999**, *63*, 1549–1557.
43. Neale, N. R.; Frank, A. J. Size and Shape Control of Nanocrystallites in Mesoporous TiO_2 Films. *J. Mater. Chem.* **2007**, *17*, 3216–3221.
44. Wen, P.; Itoh, H.; Tang, W.; Feng, Q. Single Nanocrystals of Anatase-Type TiO_2 Prepared from Layered Titanate Nanosheets: Formation Mechanism and Characterization of Surface Properties. *Langmuir* **2007**, *23*, 11782–11790.
45. Jun, Y.-W.; Casula, M. F.; Sim, J.-H.; Kim, S. Y.; Cheon, J.; Alivisatos, A. P. Surfactant-Assisted Elimination of a High Energy Facet as a Means of Controlling the Shapes of TiO_2 Nanocrystals. *J. Am. Chem. Soc.* **2003**, *125*, 15981–15985.
46. Wu, B.; Guo, C.; Zheng, N.; Xie, Z.; Stucky, G. D. Nonaqueous Production of Nanostructured Anatase with High-Energy Facets. *J. Am. Chem. Soc.* **2008**, *130*, 17563–17567.
47. Dinh, C.-T.; Nguyen, T.-D.; Kleitz, F.; Do, T.-O. Shape-Controlled Synthesis of Highly Crystalline Titania Nanocrystals. *ACS Nano* **2009**, *3*, 3737–3743.
48. Yang, H. G.; Sun, C. H.; Qiao, S. Z.; Zou, J.; Liu, G.; Smith, S. C.; Cheng, H. M.; Lu, G. Q. Anatase TiO_2 Single Crystals with a Large Percentage of Reactive Facets. *Nature* **2008**, *453*, 638–641.
49. Fang, W. Q.; Gong, X.-Q.; Yang, H. G. On the Unusual Properties of Anatase TiO_2 Exposed by Highly Reactive Facets. *J. Phys. Chem. Lett.* **2011**, *2*, 725–734.
50. Sugimoto, T.; Zhou, X.; Muramatsu, A. Synthesis of Uniform Anatase TiO_2 Nanoparticles by Gel−Sol Method: 3. Formation Process and Size Control. *J. Colloid Interface Sci.* **2003**, *259*, 43–52.
51. Sugimoto, T.; Zhou, X.; Muramatsu, A. Synthesis of Uniform Anatase TiO_2 Nanoparticles by Gel−Sol Method: 4. Shape Control. *J. Colloid Interface Sci.* **2003**, *259*, 53–61.
52. Sugimoto, T.; Okada, K.; Itoh, H. Synthesis of Uniform Spindle-Type Titania Particles by the Gel−Sol Method. *J. Colloid Interface Sci.* **1997**, *193*, 140–143.
53. Yun, H. J.; Lee, H.; Joo, J. B.; Kim, W.; Yi, J. Influence of Aspect Ratio of TiO_2 Nanorods on the Photocatalytic Decomposition of Formic Acid. *J. Phys. Chem. C* **2009**, *113*, 3050–3055.
54. Bockmeyer, M.; Löbmann, P. Formation, Densification and Properties of Sol−Gel TiO_2 Films Prepared from Triethanolamine-Chelated Soluble Precursor Powders. *J. Sol−Gel Sci. Technol.* **2008**, *45*, 251–259.
55. Lan, C.-M.; Liu, S.-E.; Shiu, J.-W.; Hu, J.-Y.; Lin, M.-H.; Diau, E. W.-G. Formation of Size-Tunable Dandelion-like Hierarchical Rutile Titania Nanospheres for Dye-Sensitized Solar Cells, unpublished results.
56. Zheng, Y.; Shi, E.; Chen, Z.; Li, W.; Hu, X. Influence of Solution Concentration on the Hydrothermal Preparation of Titania Crystallites. *J. Mater. Chem.* **2001**, *11*, 1547–1551.
57. Li, L.-L.; Chang, Y.-C.; Wu, H.-P.; Diau E. W.-G. Characterization of Electron Transport and Charge Recombination Using Temporally Resolved and Frequency-Domain Techniques for Dye-Sensitized Solar Cells. *Int. Rev. Phys. Chem.* **2012**, DOI: 10.1080/0144235X.2012.733539.
58. The electron transport and charge recombination properties of the devices are related to the structure of the TiO_2 films. To investigate the intrinsic kinetic effect of TiO_2 on photovoltaic performance, the transient photoelectric

and charge-extraction measurements were also performed for the NP and HD1 devices fabricated with similar film thickness (12−13 μm) but without adding a scattering layer and $TiCl_4$ post-treatment. The transient photocurrent decay data (Figure S11) show similar kinetic behavior as shown in Figure 6, confirming the superior electron transport ability of the HD1 film over that of the NP film as an active layer for DSSCs.

59. The effects of potential shift of TiO_2 conduction band edge and charge recombination in the dye/TiO_2/electrolyte interface for the same NP and HD devices as mensioned in ref 58 were also investigated. The charge-extraction data (Figure S12a) exhibit a potential shift of $\sim$ 30 mV between the HD1 and the NP films, which is consistent with the data shown in Figure 7a with added SL and $TiCl_4$ post-treatment. The transient photovoltage decay data (Figure S12b) show a similar behavior of charge recombination between the NP and HD1 devices, confirming that the discrepancy of V_{OC} between the two devices is due to the position of the TiO_2 potential band edge discussed in the text.
60. Ito, S.; Chen, P.; Comte, P.; Nazeeruddin, M. K.; Liska, P.; Pechy, P.; Grätzel, M. Fabrication of Screen-Printing Pastes from TiO_2 Powders for Dye-Sensitised Solar Cells. *Prog. Photovoltaics* **2007**, *15*, 603–612.